STUDY OF THE STRUCTURAL AND OPTICAL PROPERTIES OF M-TYPE $Ba_{0.75}Sr_{0.25-x}Ca_xFe_{12}O_{19}$ HEXAFERRITES SYNTHESIZED BY SOL-GEL SOLUTION COMBUSTION METHOD

PhD MINI-THESIS

BY

TESHALE WODAJE

FEBRUARY, 2024

ARBA MINCH, ETHIOPIA

STUDY OF THE STRUCTURAL AND OPTICAL PROPERTIES OF M-TYPE $Ba_{0.75}Sr_{0.25-x}Ca_xFe_{12}O_{19}$ HEXAFERRITE SYNTHESIZED BY SOL-GEL SOLUTION COMBUSTION METHOD

PhD MINI-THESIS

BY

TESHALE WODAJE

INSTRUCTOR

PROFESSOR PAULOS TADDESSE (PhD)

A MINI-THESIS SUBMITTED FOR FULFILLMENT OF REQUIREMENT FOR THE PHD INDEPENDENT SELF-STUDY COURSE (PHYS 812)

FEBERUARY, 2023

ARBA MINCH, ETHIOPIA

DECLARATION

I declare that the mini thesis titled " **study of the structural andoptical properties of m-type $Ba_{0.75}Sr_{0.25-x}Ca_xFe_{12}O_{19}$ hexaferrite synthesized by sol gel solution combustion method**" is my original work and has not been presented or submitted at any other organization or institution.

Name: _____

Signature: _____

Date: _____

ARBA MINCH UNIVERSITY

COLLEGE OF NATURAL AND COMPUTATIONAL SCIENCE

DEPARTMENT OF PHYSICS

THESIS APPROVAL SHEET

I hereby certify that the doctoral mini thesis titled "study of the structural, and optical properties of M-type $Ba_{0.75}Sr_{0.25-x}Ca_xFe_{12}O_{19}$ hexaferrite synthesized by sol gel solution combustion method " has been developed by Teshale Wodaje ID No. PRNS/078/2015 under my supervision. Accordingly, I recommend that the student has met the requirement and is hereby authorized to submit the document to the department for oral presentation.

_____	_____	_____
Name of the Instructor	Signature	Date

Approval of the Department Head

_____	_____	_____
Name of the Department Head	Signature	Date

ACKNOLWEDGMENT

First, I would like to thank the almighty God for letting me accomplish this minithesis. Secondly I would like to express my deepest gratitude to my instructor, Professor Paulos Taddesse (PhD), for his inspiration, guidance, critical comments, and unreserved support throughout my research work. His support and scientific attitude have meant a great deal to me. I would like to thank the Department of Physics for facilitating all the necessary materials to conduct my research work. I would like thanks to Arba minch University for financial support to successfully complete this self-independent study. I would also like to thank Addis Ababa and Adama Science and Technology Universities for their XRD, FT-IR, and Uv -visble spectroscopy characterization.

LISTS OF ABBREVIATIONS

FWHM	Full width at half maximum
Hc	Coercive field
JCPDS	Joint committee on powder diffraction standards
PH	Potential of hydrogen
Ms	Saturation magnetization
NPs	Nanoparticles
XRD	X-ray diffraction

TABLE OF CONTENTS

LIST OFFIGURES

ABSTRACTS

Hexagonal ferrites are used in a wide variety of current technologies due to their extraordinary magnetic properties. They are used in several applications such as military and oceanographic radar, cellular mobile, space telemetry, satellite communication and weather, automobile and so on. Recently, special attention has been given to $BaFe_{12}O_{19}$-based materials due to their potential lapplication. Some of the researchers are trying their best to improve the properties and obtain pure crystalline of doped $BaSrCaFe_{12}O_{19}$ by using different synthesis techniques. The others are trying to improve the properties of $BaFe_{12}O_{19}$ by using other techniques, such substituting cation for Ba and/ Fe sides in the $BaFe_{12}O_{19}$. This study investigates the effects of doping strontium (Sr) and calcium (Ca) into barium hexaferrite ($BaFe_{12}O_{19}$) on its structural and optical properties. Through X-ray diffraction (XRD) analysis, it is observed that doping results in an increase in lattice parameters (a) and (c), along with an expansion of the unit cell volume, while the average crystallite size decreases.

This leads to a shift towards lower wave numbers in the XRD spectrum. Fourier-transform infra-red spectroscopy (FTIR) measurements reveal that in the high-frequency range, the octahedral sites are primarily affected by the doping. Additionally, UV-visible spectroscopy indicates that the optical band gap varies with increasing calcium concentration. Overall, the doping of strontium and calcium influences both the structural and optical properties of barium hexaferrite, providing insights into its potential applications in various fields such as magnetic and optical devices.

CHAPTER ONE

INTRODUCTION

1.1. Background

Ferrites are among the most often used magnetic materials, with a wide range of applications (Ya zan et al., 2015). Among several types of innovative materials, ferrites are non-conductiveferrom agnetic chemical compounds derived from iron oxide such as hematite Fe_2O_3 or magnetite Fe_3O_4 as well as oxides of other metallic elements. Ferrites are magnetic materials which are significant class of conventional oxides due to their amazing structural and optical propertie withwide practi cal applications. Ferrite have two basic propertie which are magnetic and semiconductor nature (Ajitanshu et al.,2020). Nanostructured ferrites in the form of iron oxide system have an interesti ng research area due to their large number of unique applications such as data storage devices, co mmunication devices, and high-frequencydevices (Kar et al., 2021).

Hexagonal ferrites are divided into five sub-categories based on their crystal structure and chem-ical formula M type ($BaFe_{12}O_{19}$), W type ($Ba_2Me_2Fe_{16}O_{27}$), X type ($BaMe_2Fe_{16}O_{27}$) y type ($Ba_2Me_2Fe_{12}O_{22}$), Z type ($Ba_3Me_2Fe_{24}O_{41}$) and U type ($Ba_4Co_2Fe_{36}O_{60}$) (Gorige.et al.,2023). Among these, M-type hexaferrites have gained more attention due to their distinguished properties, such as their very high magnetic anisotropy, higher coercivity, higher corrosion resistance, and high thermal and chemical stability (Ali1et al., 2021).

M-types of ferrites such as barium ferrite ($BaFe_{12}O_{19}$), strontium ferrite ($SrFe_{12}O_{19}$), and cobalt-titanium substituted M-ferrite are ferromagnetic material with the chemical formula are in above and the space group P63/mmc (Basha et al., 2022). The majority of hexa-ferrite research focuses on the complex structure, qualities that are altered by the substitution of various magnetic and non-magnetic ions at these sites can modify the structural, and opical properties of BaM ferrites (Virender et al. ,2018). These parameters can be controlled by the substitution of ions in their formula, as mentioned above, but also by the variation of pH, temperature, grain size, reaction speed and heat treatment time, through different synthesis methods (Ayan et al.,2019).

However, $BaFe_{12}O_{19}$, highly depends on the type of dopant, sintering temperature, and synthesis method. Properties of $BaFe_{12}O_{19}$ based hexaferrites at high frequencies were implemented in mic

rowave absorbing characteristics, which are influenced by the complex values of permeability and permittivity (Popap *et al.(* 2005).

Due to structural and optical properties, $BaFe_{12}O_{19}$-based hexaferrites have been using for the combination of structural and optical properties in $BaFe_{12}O_{19}$ hexaferrites enables their use in magneto-optical devices, including magneto-optical recording media, sensors, and isolators. (Poo ja et al., 2021). To day, various techniques but most often chemical syntheses methods for prepar ing magnetitenparticles already have been reported, as the co-precipitation, and high temperature organic phasedecomposition (Slimani.Y et al.,2021). Sol-gel method is known for mixingof part-icles of in organic or metallo-organic precursors on the colloidal scale. Sol gel method involves mostly mixingof metal nitrates in desired solvent followed by continuous stirring of the solution (Syahwina et al., 2017). The advantages of the sol gel method include the high homogeneity of the resulting material singephase crystal structure the ability to control the particle size, and the stoichiometriccomposition. Due to features of the method, the energy consumption is reduced. However, the most significant advantage of the sol-gel method is the mechanical properties of sols and gels, soit can be used obtain fibers, needles, films, and composites that can be deposited on the surface. In this study, $Ba_{0.75}Sr_{0.25-x}Ca_xFe_{12}O_{19}$ (0.0, 0.05, 0.1, 0.15, and 0.25) hexaferrite would be synthesized by sol-gel synthesis method. Their structural and optical properties would be investigated using different advanced characterization techniques, such as X-ray powder diffraction (XRD), Fourier transform infrared (FTIR) spectroscopy.

1.2. Statement of problems

Recently, ferrites materials have been used in a wide range of industrial and technological applic ations in the field of electronic devices, loud speaker, recorder, magnetic storage device and elec-tric motor and so on with controlling the size of materials (Ertuğ et al. ,2021). Typically, M-type of barium hexaferrite has gains many researchers attention due to their low production cost, low density,simple and easy, thermal stability, the existence of large saturation magnetization high coercive field, very low electrical conductivity mechanical hardness, corrosion resistivity high microwave magnetic loss moderate permittivity(Maramu et al.,2021). However, Barium ferrites are hard magnetic property which limited available for enhancing structural, and property due to small surface area to volume ratio and atoms are inside the surface rather than on the surfaced Banihashemi V et al. (2020).

In order to get high-powered barium based hexaferrites, researchers have used different synthesis techniques, such as hydrothermal, sol-gel combustion, salt melting techniques. Among this sol-gel synthesis method is selective synthesis due to simplicity, cost effective and homogenous solution. In addition, this synthesis method has the advantages in producing nanosize products. Considering this unique method researchers have been done enhance structural parameters and magnetic property with substitutions various elements in $BaFe_{12}O_{19}$ (Syukur Daulay1 et al.,2019) In this research, the structural and optical properties of M-type nanocrystallin $BaFe_{12}O_{19}$ and hex aferrites would be investigated using XRD, FT-IR and Uv visible spectroscopy

1.3. Objectives of the study

1.3.1 General objective

The general objective of this mini this work is to study of structural and optical properties of $Ba_{0.75}Sr_{0.25-x}Ca_xFe_{12}O_{19}$ (0.0, 0.05, 0.1, 0.15, and 0.25) nanohexaferrites prepared by sol gel combustion method.

1.3.2 Specific objectives

- To synthesize phase pure $Ba_{0.75}Sr_{0.25-x}Ca_xFe_{12}O_{19}$ nanohexaferrites by using sol gel combustion method.
- To identify the crystal structure, phase formation, of all samples using XRD, and FTIR spectroscopy.
- To investigate the structural properties of the synthesized hexaferrites by using XRD and FT-IR
- To estimate the structural and optical parameters of all samples.

1.4 Significance of the study

Barium hexaferrites possess highly potential structural and optical properties and are the most preferred materials in technological applications. In the present work, the crystal structure of $Ba_{0.75}Sr_{0.25-x}Ca_xFe_{12}O_{19}$ barium hexaferrites would be investigated. For this purpose, different advanced instruments like XRD, FT-IR and Uv visible spectroscopy, and others would be utilize Different parameters like structure would also be evaluated from the obtained data. It is believed that this work would be provided a significant contribution towards a better understanding of the

materials to be investigated. Moreover, the findings of this study would be also contributed to fut ure research in the field of nanohexaferrites with a focus on achieving good physical properties for technological applications.

CHAPTER TWO

Crystal Structure of M-type hexaferrite

2.1 Structure of barium hexaferrite

There are six types of hexaferrite such as M, Y, W, Z and X are summarized blow in the table 2.1 and the structure of hexaferrite are classified as two. The structure of hexagonal can be descri bed by the two approaches such as spinel-based model and block-based model.

2.1.2 Spinal based system

The structure of the hexaferrites the some to that of the spinal ferrite structure which is composed of the plates close packed cubic oxygen with similar metal ions and these metal ions are present at the octahedral and tetrahedral interstices.

The small intervening space between these layers is filled with three octahedral or one octahedral and two tetrahedral sites and the spinel structure is obtainned by the layers of four oxygen atoms repeating three vertical layers to form an ABCABC lattice from the Fig 2.1

The structure of the hexaferrites the some to that of the spinal ferrite structure which is composed of the plates closed packed cubic oxygen with similar metal ion and this metal ion are present at the octahedral and tetrahedral interstices (Packiaraj.G et al., 2020). . The small intervening space between these layers are filled with three octahedral or one octahedral and two tetrahedral sites and the spinel structure is obtained by the layers of four oxygen atoms repeat three vertical layers to form an ABCABC lattice. The hexaferrite have two types of the plates ($S_4$and S_6) are presents which are joined two barium containing layers ($B_1$and b_2)in which the M,Y and Z consis t one only plates (s_4),W structure consist of only one plates(S_6) and the X structure consist of two plate ($S_4$and S_6. B_1 layer appears in case of M, W, Z ferrites, is a single hexagonal layer which contains the barium atom in position of four oxygen atoms and the B_2 layer appears in case of Z ferrites is two hexagonal layers which contain the two barium atoms in position of eight oxygen atoms.

Table2.1. The six type of hexaferrite.

Ferrite	Formula	Spinel plates and hexagonal layers	S/R/T structure
M	$BaFe_{12}O_{19}$	$2M5=B_1S_4B_1S_4$	SR S*R*
W	$Ba_2Me_2Fe_{16}O_{27}$	$2W7=B_1S_6B_1S_6$	SSRS*S*R*
X	$BaMe_2Fe_{16}O_{27}$	$3X_{12} = B_1S_4B_1S_6B_1S_4B_1S_6B_1S_4B_1S_6$	SSRS*S*R*
Y	$Ba_2Me_2Fe_{12}o_{22}$	$2Y_6 = B_2S_4B_2S_4B_2S_4$	3 (ST)
Z	$Ba_3Me_2Fe_{24}o_{41}$	$2Z_{11} = B_2S_4B_1S_4B_2S_4B_1S_4$	STSRS*T*S*R*
U	$Ba4Co2Fe_{36}O_{60}$	$U_{16} = B_1S_4B_2S_4B_1S_4$	SRS*R*S*T*

Table 2.1 shows the basic properties the six types of hexaferrite where * represents 180° rotation of block around the c-axis. The metal ions are present at the divalent and trivalent interstices. The interstices between these layer are filled with three interstices octahedral or one octahedral and two tetrahedral sites and the spinel structure is obtained by the layers of four oxygen atoms repeat three vertical layers to form an ABCABC lattice. In the hexagonal ferrites, two types of plates (S_4 and S_6) are present which are joined together by two barium containing layers ($B_1$and B_2) in which the M, Y and Z consist of only one plate (S_4), W structure consist of only one plate (S_6) and the X structure consist of two pates (S_4 and S_6). B_1 layer appears in case of M, W, Z ferrites, is a single hexagonal layer which contains the barium atom in position of four oxygen atoms and the B_2 layer appears in case of Z ferrites is two hexagonal layers which contain the two barium atoms in position of eight oxygen atoms

2.2.3 Hexagonal ferrites

Hexagonal ferrites are widely used as permanent magnet and are characterized by possessing a high coercivity. They are used at very high frequency region. Their general formula is $MFe_{12}O_{19}$ where M is an element like Barium, Lead or Strontium .The hexagonal ferrite lattice is similar to the spinel structure, with the oxygen ions closely packed, but some layers include metal ions, which have similar ionic radii as the oxygen ions. This lattice has three different sites occupied by metals: tetrahedral, octahedral and trigonal bi-pyramid .There is six types of HFs indicated by M, W, Y, X, Z, and U letters . M, W, Y, X, Z and U consist of (MO + MeO) and Fe_2O_3 in the ratios, where M could be the Ca, Sr, Pb, Ba, La ions, Me is a transition cation

(Mg, Zn, Mn, Co) or a combination of cations similar to the spinel. The Furthermore, the replace ment of Fe^{3+} ions with other cations such as $Ga^{3+,}$ Al^{3+} Sc^{3+}, In^{3+} is also possible. The crystalline structure of the HFs is the result of the close packing, of oxygen ion layers. The divalent and trivalent metallic cations are located in interstitial sites of the structure, while the heavy Ba or Sr ions enter in the oxygen layers. All the known HFs have a crystalline structure consisting of the superposition of three fundamental structural blocks namely S-block, R -block, and T block.
While the heavy Ba or Sr ions enter in the oxygen layers. All the known HFs have a crystalline structure consisting of the superposition of three fundamental structural blocks namely S-block, R-block, and T-block.

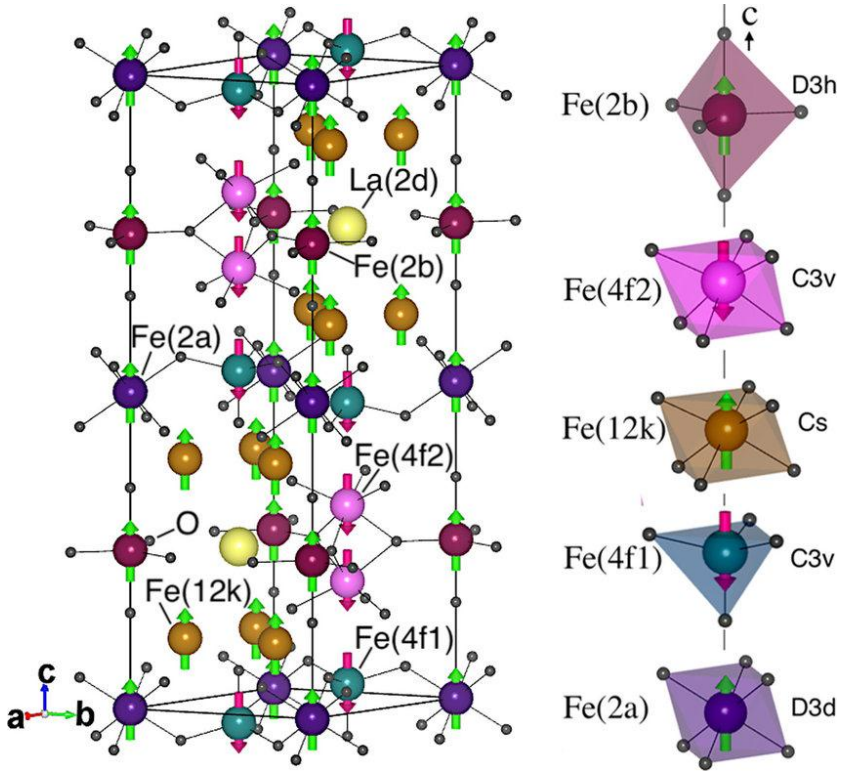

Figure 2.1. Crystal structures of (a) two layers of S block, (b) R block and (c) T block

2.3. Structure of barium ferrites

The M-ferrite is type of hexagonal ferrite which is composed of one S block and one R block. These blocks are overlapped with hexagonally and cubic packed layers and also, the plane which contains the barium atom is called mirror plane where the S and R blocks are 180˚ rotation around the c-axis, so, the mirror block R, R* providing the unit cell formula SRS*R* where * shows the 180˚ rotation of the given block around the c-axis . Also, it was demonstrated that the

BaM ferrite composed of stacking of spinel like blocks and substituted M-type ferrite has been investigated on large scale such as $BaFe_{12-X}A_XO_{19}$ (Delacotte.C et al., 2018). This has been investigated for improving the magnetic properties of BaM ferrite. The grain size of synthesized specimens decrease obviously with increase of Ba/Fe ratio $BaFe_{12}O_{19}$ has a hexagonal crystalstr ucture, belonging to the magnetoplumbite crystal containing"R" block ($(BaFe_6O_{11})^{2-}$) and cubic "S" block ($(Fe_6O_8)^{2+}$) in c-direction. When these blocks are cause to move in a circle aroundan axis by 180°, they will be denoted by S∗ and R∗ with a constitutional unit cell (SG :P63/mmc,a= 0.588 nm,c = 2.318 nm) preferred axis c-direction where all loose crystals can easily align along the c -axis parallel to the magnetic field. Finally, the stacking of an R and an S block prod-uces an M unit block Fig 2.1

2.4. Optical properties $Ba_{0.75}Sr_{0.25-x}Ca_xFe_{12}O_{19}$

UV–vis spectroscopy obtains the absorbance spectrum of a molecule or compound in solution or solid form. Electrons in the ground state are stimulated to excited-state levels by electromagnetic radiation. The UV-visible portion of the electromagnetic spectrum has a wavelength range of 800 nm to 200 nm, or 1.5 eV to 6.2 eV in terms of energy. The Beer-Lambert Law is the foundation of absorbance spectroscopy. Lambert's law states that "when a light beam passes through a clear medium, the decrease in light intensity is precisely proportionate to the medium thickness (Ibrahim Mohammed et al. , 2023)

When the light irradiates on the surface of the material the phenomena of light reflection and absorption occur (Chapa Pamodani. A. et al.,2024). The band gap energy and the optical property of the as-prepared material were measured by using an UV-Visible diffuse reflectance spectrometer at room temperature in the wavelength range of 200 to 800 nm. When radiation is incident on materials capable of conducting current, electrons in the valence band absorb energy from the radiation. This absorbed energy allows them to move to higher energy levels (conduction band). This energy therefore corresponds to the energy difference between the valence band and conduction band and defines the band gap calculated by the following relation. (Agrawal et al. , 2021).

CHAPTER THREE

MATERIALS SYNTHESIS AND METHODS

3.1 Chemicals list

Table 3.1 shows those chemicals that would be used for this research. The chemical formula of the raw materials together with their purpose, impurity percentage, and suppliers are also included in the table.

Table 3.1. List of chemicals to be used for synthesizing of all samples.

Name of chemical	**Chemical Formula**	**Purpose**	**Purification (%)**	**Chemicals per used from**
Barium nitrite hydrated form	$Ba(NO_3)_2$	source of (Ba)	99	Merck, India
Ferric Nitrite hydrated from	$Fe(NO_3)_3.9H_2O$	source of (Fe_2O_3)	99	Merck, India
Strontium Nitrite hydrated from	$Sr(NO_3)_2$.	Source of Strontium(Sr)	99	Merck, India
Calcium nitrite hydrated form	$Ca(NO_3)_2.4H_2O$	Source of calcium(CaO)	99	Merck, India
Citric acid hydrated form	$C_6H_8O_7.H_2O$	chelating agent for the chemical reaction	99.5	Merck, India
Ammonia solution	NH_3	To control the P^H values	25	Merck, India
Deionizer water	H_2O	To dissolve the solution		

3.2. Materials synthesis

3.2.1. Synthesis of $BaSCFe_{12}O_{19}$ hexaferrites

To synthesis $BaFe_{12}O_{19}$ nanohexaferrite, sol-gel combustion method would be employed. Ba $(NO_3)_2$, Fe $(NO_3)_3.9H_2O$ and $C_6H_8O_7.H_2O$, raw materials would be used without further purification The metal nitrates would be mixed and dissolved it in 60 ml amount of distilled water. Further, a stoichiometric amount of citric acid would be dissolved in 30 ml distilled water in a separate beaker. The individual solution would be mixed together in one beaker. The aqueous solutions of the metal nitrates and citric acid would be mixed molar ratio of 1:3. The solutionwould be stirred for 30 minutes using a magnetic stirrer. Next, liquid ammonia would be added drop wise to maintain a pH level of 7 in the solution. After that, solution would be heated to 90˚C with vigorous stirring until a sol is formed. Further heating to 100°C would be carried out to produce a dry gel, leading to combustion. The resulting black powder would be ground for approximately four hour s using an agate mortar and pestle. The obtained powder would be transferred into alumina cruci bles and calcined at 1100 ^oC for 4 hours in a muffle furnace at a heating and cooling rates of 5 °C /minute. Finally, the calcined powder would be ground for about one hour to obtain the desired particles. The synthesis procedures are illustrated in Figure 2.1.

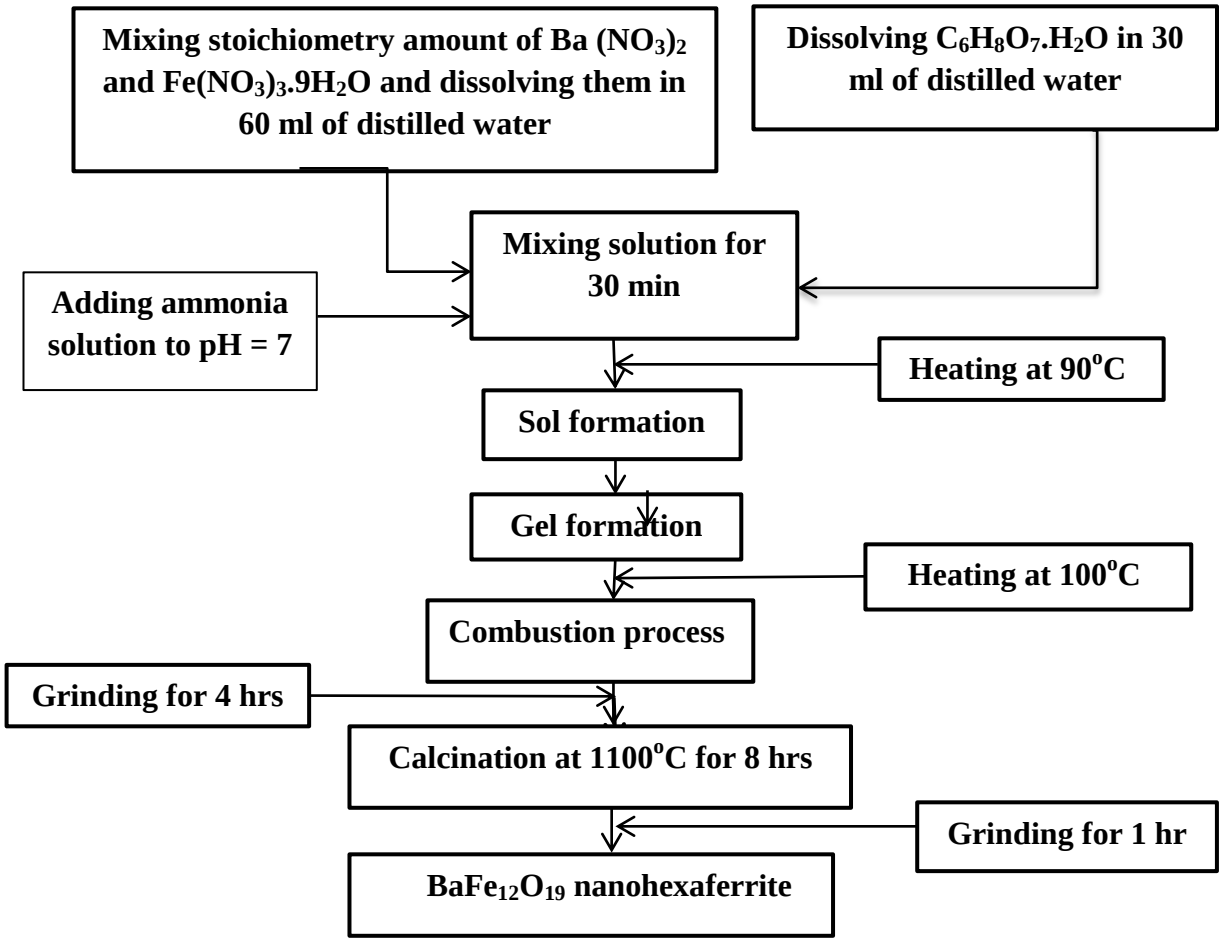

Figure 3.2: Producers for synthesis of $BaFe_{12}O_{19}$ hexaferrite.

Similarly, $Ba_{0.75}Sr0._{25-x}Ca_xFe_{12}O_{19}$ nanohexaferrite would be also be synthesized by sol-gel com bustion method using Ba $(NO_3)_2$, $Sr(NO_3)_2$, Ca $(NO_3)_2.4H_2O$, and $Fe(NO_3)_3.9H_2O$ raw materials. The $C_6H_8O_7.H_2O$ would be used as a fuel and chelating agent during the synthesis process.

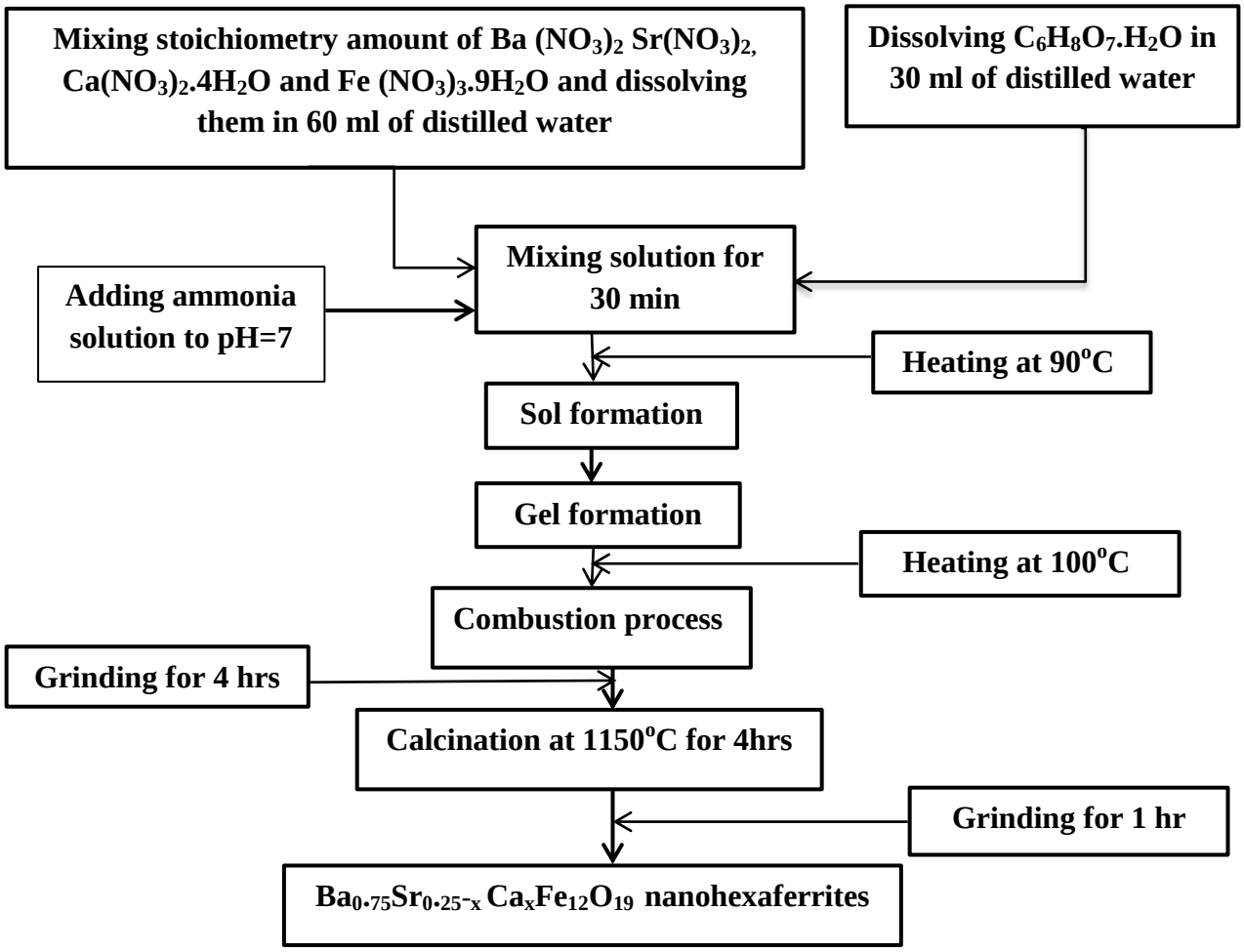

Figure 3.3: Producers for synthesis of $BaSrCaFe_{12}O_{19}$ hexaferrite.

After this, the same procedures would be utilized as for synthesizing $BaFe_{12}O_{19}$ hexaferrite. The synthesis procedure is illustrated in Figure 2.2.

Figure 3.4: Producers for synthesis of $Ba_{0.75}Sr_{0.25-x}Ca_xFe_{12}O_{19}$ hexaferrites (Misbah et al ., 2022)

3.3. Materials characterization techniques

3.3.1. X-ray powder diffraction

X-ray diffraction (XRD) is a powerful nondestructive technique for characterizing crystalline materials. It provides information on structure, phase, preferred crystal orientations (texture),and other structural parameter, such as average grain size, crystallinity, strain, and crystal defect. The peak intensities are determined by the distribution of atoms within the lattice. Consequently, the X ray diffraction pattern is the fingerprint of periodic atomic arrangements in a given material. X-ray diffraction analysis were performed using a shimadzu X-ray diffractometer (XRD 6100) equipped with CuKα radiation (λ=1.5406Å). Each sample where scanned the 2θ range of 20-80°. The XRD patterns of all the compositions were recorded at room temperature. The diffraction

angle, 2θ, the wavelength of the x-rays and the inter planar separation d of the diffraction planes within the crystal are related through the **Bragg** diffraction condition, that is,

$$2d\sin\theta = n\lambda \qquad n = 1, 2, 3 \qquad (1)$$

where d is the inter-planar distance, θ is the Bragg angle, n is the order of the diffraction and λ is the wavelength of the incident wave.

The unit cell lattice parameter a, is given by using following relation

$$\frac{1}{d^2} = \frac{4}{3}\left(\frac{h^2+hk+k^2}{a^2}\right) + \frac{h^2}{c^2} \qquad (2)$$

The average crystallite size of the samples is given Scherer's formula [30];

$$D = \frac{0.9\lambda}{\beta \cos\theta} \qquad (3)$$

Where λ is the X-ray wavelength, θ is the Bragg diffraction angle, and β is the (full width half maxima) FWHM of the XRD peak appearing at the diffraction angle θ.

The unit cell volume of the all samples is calculated by;

$$V = 0.866a^2c\ (\text{Å})^3 \qquad (5)$$

Magnetic moments in the absence of an external magnetic field. Above the Curie temperature the susceptibility follow relationship (4) with a negative sign. When temperature approaches TC the magnetic susceptibility tends to be infinite. The susceptibilities of ferromagnetic materials are typically of order 10^3 or 10^4 or even greater than. The atomic dipole moments in these materials are characterized by very strong positive interactions. .

3.3.2. Fourier transforms infrared (FT-IR) spectroscopy

Fourier transforms infrared (FT-IR) spectroscopy it is the most important characterization techni que which is sensitivity and relatively a few time for tests. In FT-IR spectroscopy measures, IR radiation is transfer through a sample and some of the infrared radiation is absorbed by the sample and another of it is transmitted through the sample.

The next the spectrum can be represents the molecular absorption and the transmission, creating a molecular fingerprint of the sample. Like a fingerprint no two unique molecular structures produce the some infrared spectrum. FT-IR measuring technique would be made using the pellet samp

les from potassium bromide (KBr).The measurements would be accomplished using transmittance method in the wave number region of 400 -4,000 cm^{-1}using (IRPrestige-21 Shimadz instrument). In preparing samples for FT-IR investigation, the powder sample would be grid agate mortar for about 10 minutes.

3.3.3. UV–visible spectroscopy

Ultraviolet–visible spectroscopy it is characterization technique which is used to study the optical properties, such as the optical band gap and refractive index of materials. The term “band gap” refers to the energy difference between the top of the valence band to the bottom of the conduction band; electrons are able to jump from one band to another. In order for an electron to jump from a valence band to a conduction band, it requires a specific minimum amount of energy for the transition, the band gap energy. The optical energy band gaps of these materials were determined using the fundamental absorption, which corresponds to electron excitation from the valance band to the conduction band using Tauc‟s relation;αhν= A (hν -)n where hν is the excitation energy, is the energy band gap ,A is the absorption constant, is the absorption coefficient and the exponent n is used to determine the type of electronic transition and takes values of 1/2 or 3/2 for direct transitions, whereas for indirect transitions, n is equal to 2 or 3, depending on whether they are allowed or forbidden, respectively.

CHAPTER FOUR

RESULTS AND DISCUSSION

4.1. X-ray diffraction (XRD)

The x-ray diffraction XRDpattern of $Ba_{0.75}Sr_{0.25-x}Ca_xFe_{12}O_{19}$ (x = 0.0, 0.05, 0.1, 0.15, and 0.25) samples sintered at 1150 °C are shown in the figure 4.1. All the observed peaks were indexed and compared to the X-ray diffraction XRD patterns obtained from M-type barium hexaferrite a shimadzu X-ray diffractometer (XRD 6100) equipped with CuKα radiation (λ=1.5406Å). Each sample where scanned in the 2θ range of 20-80 and the observed peaks in the figure 4.1 from (a)-(e) are well indexed by the hexagonal indices of $Ba_{0.75}Sr_{x-02}CaFe_{12}O_{19}$ (JCPDS No 00-05-1879) with *P63/mmc* space group Awad et al. (2019). Analysis of all the XRD patterns confirms that no impurity phase are present in the samples such as $Ba_{o.75}Sr_{0.25}Fe_{12}O_{19,}$ $Ba_{o.75}Sr_{0.5}Ca_{0.2}Fe_{12}O_{19}$, $Ba_{o.75}Sr_{0.1}Ca_{0.15}Fe_{12}O_{19}$, $Ba_{o.75}Sr_{0.15}Ca_{0.1}Fe_{12}O_{19}$ and $Ba_{o.75}Ca_{0.25}Fe_{12}O_{19}$ have high purity and high crystallinity. The sharp and single diffraction peaks indicate good homogeneity and crystallinity of the sample (Murli Kumar et al., 2021).

A comparison of the obtained data with the diffraction pattern of doping strontium and calcium on $Ba_{0.75}Sr_{x-0.25}Fe_{12}O_{19}$ showed that the samples with an *x* value ranging from (x = 0.0, 0.05, 0.1, 0.15, and 0.25) comprise a single phase when the value of the x increase means the value of the strontium the particle size would be increase and when the concentration of calcium increase the particle size would be decrease properties (Yinghui .Z. et al. ,2021)..

The broad peaks of X-ray diffraction patterns stipulate that the particles of the synthesized samples are in nanometer range. The average crystallite size of the samples could be calculated by Scherrer's formula, which depends on the peak boarding of the X ray peaks. Peak boarding comes due to many factory finite crystallite size, instrumental effect, and strain effect within lattice. Scherrer's formula define as

$$D = \frac{(0.9*\lambda)}{\beta cos\theta} \quad \text{..... (6)}$$

The calculated average crystallite sizes for the system $BaSr_{x-1}Ca_xFe_{12-x}O_{19}$ with (sintered at T = 1150 ℃. The average crystal size were found to be in the range of (47.-43.2) nm for samples sintered at 1150 ℃, where λ is the X-ray wavelength (CuKα radiation and equals to 0.154 nm),

θ is the Bragg diffraction angle, and β is FWHM of the XRD peak appearing at the diffraction angle θ (Erfan Handoko et al., 2020). The average crystalline size was calculated from the X-ray line broadening using

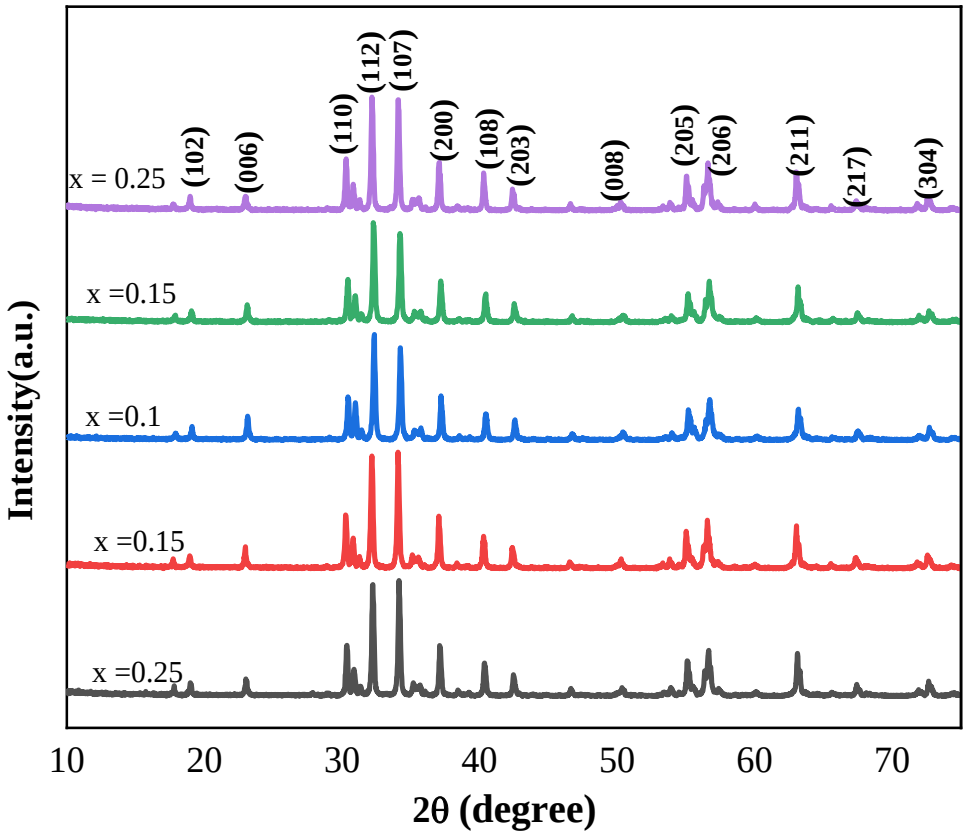

Figure 4.1: XRD patterns of the $Ba_{0.75}Srx_{-0.25}Ca_{-x}Fe_{12}O_{19}$ ferrite hexaferrite powders Sr-Ca ion concentrations

Based on Bragg's Law, the plane spacing of hexagonal crystal, *d* is related to the lattice parameters (*a and c*) as shown in Equation

$$\frac{1}{D^2} = \frac{4}{3} * \frac{h^2+hk+k^2}{a^2} + \frac{l^2}{c^2} \quad \text{.....(7)}$$

Table 4.1 Structural parameters, c/a ratio, unit cell volume v ($\dot{A}^3$) X-ray density (Dx) the average grain size (Dav) are listed (VERMA et al., 2023)

Sr-Ca concretion	a(Ȧ)	c(Ȧ)	v($Ȧ^3$)	c/a	Dav(nm)	X ray density
Sr (0.25), Ca (0.0)	5.83	23.372	687.884	4.14	47.9091	5.19
Sr (0.2), Ca(0.05)	5.842	23.390	690.83	4.008	44.67	5.18
Sr(0.15), Ca(0.01)	5.851	23.417	693.7	4.002	43.7746	5.19
Sr(0.1), Ca(0.15)	5.856	23.421	695.5	4.212	43.7746	5.18
Sr(0.0), Ca(0.25)	5.857	23.441	696.3	4.002	43.235	5.17

As the table shown above that the lattice constant of $Ba_{0.75}Sr_{0.25-x}Ca_xFe_{12}O_{19}$ found the range from 5.83-5.857 (Ȧ) for (a) and 23.372-23.857 (Ȧ) for (c) parameter. The variation of lattice con stant(a), (c) as the function of the (Sr) and calcium (Ca) concentration .These values are found to be in good agreement with the reported lattice parameters of the value of a and c Brightlin,. 2016 shows that both the lattice parameters "*a*" and "*c*" increasing amount of calcium (Ca^{2+}) content and decrease the amount of strontium. This can be attributed to different ionic radius of Sr 1.18 (Ȧ) compared with that of Ba^{+2}(1.35Ǻ) and Ca with ionic radius of (0.997Ȧ) respectively (Erfan Handoko et al., 2020). The lattice parameter a and c increase with increase in the concentr ation of Ca ion. To decrease the concentration of strontium also lattice constant decrease. This is due to relatively small ionic radius of Ca^{+2} (0.99 Å) comparing to that of Fe^{3+} (0.645 Å) for six fold coordination (Martirosyan .K.Set al., 2010). The crystallite size of the sample with the concentration of calcium increase the particle size decrease and the particle size increase with concentration of the strontium decrease. Calcium ions, being smaller in size compared to strontium ions, may facilitate more effective nucleation and hinder the growth of crystallites. This can lead to a reduction in the average crystallite size as the concentration of calcium increases. Strontium ions, being larger in size compared to calcium ions, may promote the growth of larger crystallites by providing more space for atoms to arrange themselves in the crystal lattice(Emre Burak et al., 2016)..

$Ba_{0.75}Sr_{0.25-x}Ca_xFe_{12}O_{19}$ while it reaches its highest value (47nm) at x=0.25, due to the presence of the strontium ion next to the calcium, which accelerates the growth of crystallite sizes. While

X-ray density decreases linearly with increasing Ca- ion concentration. This is due to the ionic radius Ca^{+2} is smaller than that of Sr^{+2} ion (Ghulam Asghar,et al., 2020).

There is no change in thebasic hexaferrite structure. However, a slight shift in the peak position t he some change in the intensity of few reflection have been observed in the figure 4.3 (b)

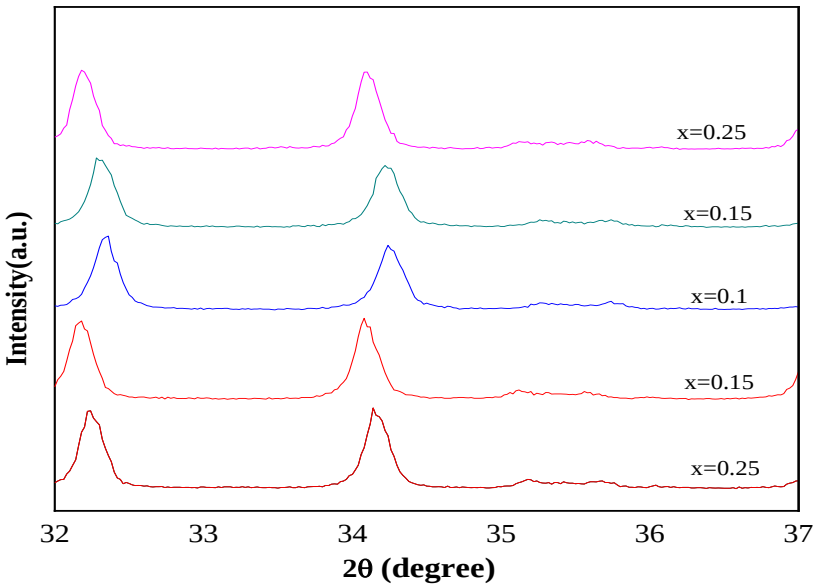

Figure 4.2: XRD pattern of BSCFO compound with different doping content in (a) 20◦ -80◦ range and (b) close up view in 32◦ -37◦ rang

The lattice parameters were determined using cell software. It was observed that by doping of Mg^{2+} and Mn^{3+}, the lattice parameters changed significantly. This may be due to substitution of larger ionic radii with smaller ionic radii, that is, Sr^{2+} (1.18A°) and Ca^{3+} (0.99A°) ions have larger ionic radii compared to Fe^{3+} (0.76A°) and Ba^{2+} (1.35A°). It was also observed that the diffracted peaks shifted toward the lower 2θ values as the Sr and Ca content was decrease or increase , which may be due to stress produced in the crystal lattice and the expansion of unit cell parameters. Since the stress is due to the change in the ionic radii of the dopant ions and host metal ions, which might cause distortion in the crystal lattice at various degrees (Ismat Bibi et al.,2021). When smaller ionic radii were interchanged with larger ionic radii, stress or distortion is produced in the crystal structure; therefore, cell volume increased from 540 to 590 (A^3) and these observation

correlates well with earlier studies. The X-ray density, cell volume, and lattice parameters for the prepared samples are depicted.

4.2. Fourier transforms infrared (FT-IR) spectroscopy analysis

This device produces a signal that contains all infrared frequencies. It is possible to monitor this signal very quickly, typically in less than a second. As a result, infrared spectroscopy has greatly benefited from the FT-IR technique (Yinghui .Z. et al. ,2021. It has made it possible to create a number of cutting-edge sampling techniques to deal with challenging circumstances that earlier technology was unable to resolve. The FTIR spectrum of the $Ba_{0.75}Sr_{0.25\ -x}Ca_xFe_{12}O_{19}$ (x = 0.0, 0. 05, 0.1, 0.15, and 0.25) FT-IR measuring technique would be made using the powder samples. The measurement can be accomplished using transmittance method in the wave number region of 400-4,000 cm^1 using (IRPrestige-21 Shimadz instrument) in the figure 4.3. It has been reporte that the IR bands of solids are usually attributed to the vibration of ion in the crystal lattice. Shows room temperature FTIR spectra for $BaFe_{12}O_{19}$, and $Ba_{0.75}Sr_{0.25\ -x}Ca_xFe_{12}O_{19}$ (x = 0.0, 0.05 ,0.1, 0.15, and 0.25 with samples calcined at 1150°C. The strong absorption peaks between 590 cm^{-1} and 432 cm^{-1} confirm the formation of hexaferrite phase (Charmi .D et al. ,2020). .
Two frequency band confirmed the higher frequency band (v_1) (432-440 cm^{-1}) and lower frequen cy band (v_2) (551-590 cm^{-1}) are assigned the tetrahedral and octahedral site are assigned to Fe-O bending vibration and Fe-O starching vibration, respectively (Pullar.,2012).Clear from the figure 4.3 show the single hexagonal structure with the formation two kind of characteristic absorption bands. Thus, the formation of a single phase hexagonal structure of ferrite was confirmed to clear the hexagonal structure with the two type of characterization absorption band are formed from the 432-440cm^{-1} for tetrahedral and 551-590 cm^{-1} for the octahedral (Widyastuti et al. , 2017). These were associated with stretching vibration of tetrahedral (A) site and octahedral (B) site. It can be observed from the IR plots that the band positions and changes slightly. This may be due to the distribution of Sr and Ca ionic radius(1.18 and 0.99) which are replacing by Fe Peaks at 432 cm^{-1} and 580 cm^{-1} are assigned to magnetite vibration bonds of Fe–O at tetrahedral and octahedral sites. It is obvious, from figure 4.3 (c), that the peaks position of the pure sample (x= (0.05, 0. 01) is not altered or shifted after Calcium additions.
Moreover, the influence of calcination temperature on $BaSrCaFe_{12}O_{19}$structure is displayed in figure 4.3 (b) for $BaSrCaFe_{12}O_{19}$ with x= (0.1) (Sonals.S et al. 2017). For instance, the peak that

defines the stretching vibration bonds of Fe–O at the tetrahedral site changed from 432 cm^{-1} to 580 cm^{-1} as the calcination temperature is 1150 °C.

The strong absorption peaks between 580 cm^{-1} and 432 cm^{-1}confirm the formation of hexaferrite phase and the second observation is 541 cm^{-1} to 526 cm^{-1} was assigned to the Sr-O bending vibra tion (Bayka .A et al., 2016).

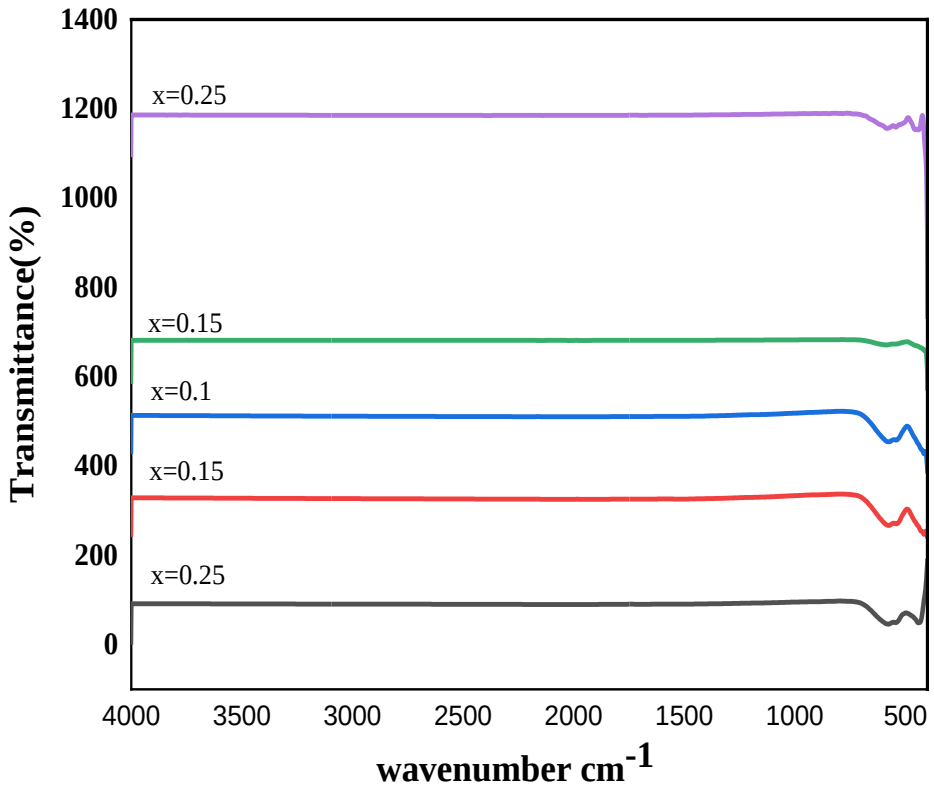

Figure 4.3: FT-IR spectra of $Ba_{0.75}Sr_{x-0.25}Ca_xFe_{12}O_{19}$ nanohexaferrites

The formation of these bonds with corresponding frequency modes confirms the presence of metal-oxygen (M-O) stretching band in hexaferrite structure (Vadivelan et.al., 2016) All absorption bands broadened along with a shift to lower wavenumber with the increase in the Ca^{2+}-Sr_{3+} content in the compound. This shift in the band position to lower wavenumber is due to increased frequency of vibrations upon substitution of lighter Ca and Sr atom for heaver Sr and Fe atoms doping (GHULAM et al. , 2020).

Table the absorption FTIR bands of Ba1-xSrxFe12O19

Sample	Wave number		
	V_1	V_2	V_3
$Ba_{o.75}Sr_{0.25}Fe_{12}O_{19}(S_1)$	440	541	576
$Ba_{o.75}Sr_{0.5}Ca_{0.2}Fe_{12}O_{19}(S_2)$	432	540	570
$Ba_{o.75}Sr_{0.1}Ca_{0.15}Fe_{12}O_{19}(S_3)$	442	541	587
$Ba_{o.75}Sr_{0.15}Ca_{0.1}Fe_{12}O_{19}(S_4)$	432	551	580
$Ba_{o.75}Ca_{0.25}Fe_{12}O_{19}S_5$	432	551	590

The lower wavenumber band (v_1 and v_2) is attributed to the tetrahedral vibrations, while the higher bands (v_3) are ascribed to the octahedral vibration.

4.3 Optical Band gap Studies

When characterizing optical properties of M-type hexaferrite using UV-Vis absorption technique two distinct optical transitions (i.e. direct and indirect) may occur near the basic absorption edge of the materials. The band gap energy and, therefore, the optical property of the as-prepared material were measured by using a UV-Visible spectrometer at room temperature within the wavelength range of 200 to 800 nm. The optical absorption of the ferrite nanoparticles is very important because of the UV–vis absorption edge, which is related to the band gap energy of the photo catalyst (Shu.R.et al., 2020.

From the figure 4.4 , one can easily conclude that the absorption magnitude of co-doped ensembles are up to 25% larger with respect to absorption of un doped $Ba_{0.75}Sr_{0.25-x}Fe_{12}O_{19}$ samples in the photometer's sweep range between 200 nm and 800 nm (Tchouank.T., 2020). On the contrary, the absorption magnitudes of un doped $Ba_{0.75}$ $Sr_{0.25-x}Fe_{12}O_{19}$ samples are remarkabl y higher Nanomaterial than the absorption of co-doped BHFs above 650 nm.

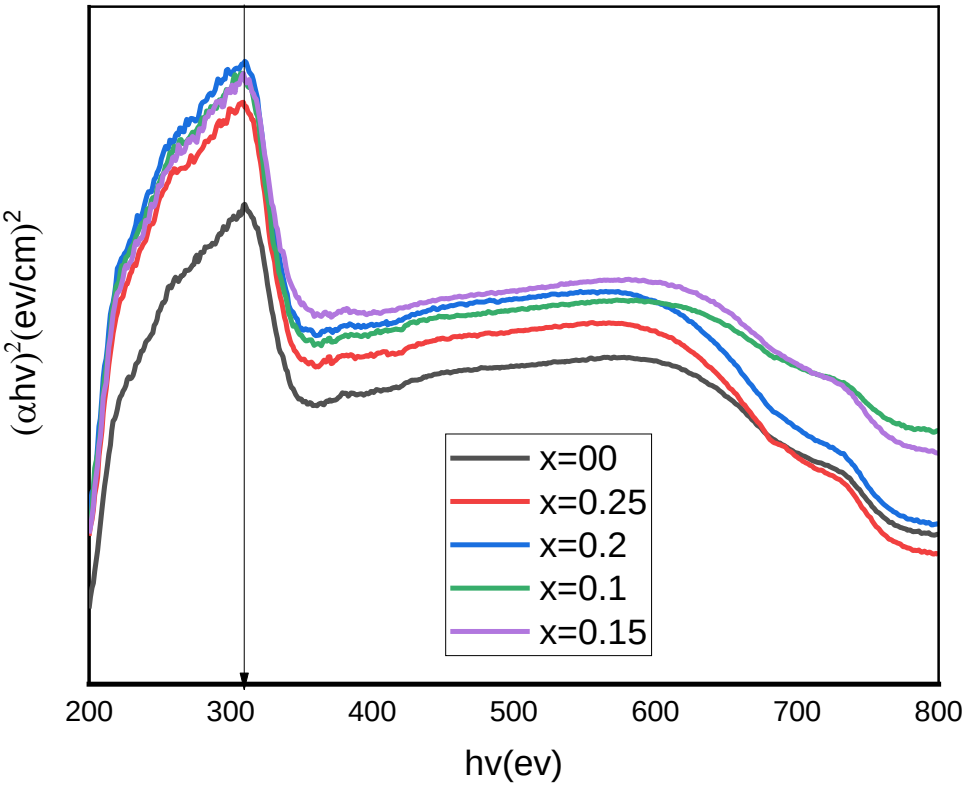

Figure 4.4: Absorption spectra of the $Ba_{0.75}Sr_{0.25-x}Ca_xFe_{12}O_{19}$ hexaferrite

where hv is the incident photon energy and A is a constant number; therefore, the band gap has been calculated by extrapolating the linear region of plots $(\alpha hv)^2$ vs hv on the energy axis. The band gap value can be calculated from the graph range of 2.77 eV to 3.08 eV which matches well with the previously reported value (Mahapatro, 2021). The effects of dopant on the energy band gap were investigated and the results revealed that by increasing and decreasing the dopant content of Ca and Sr, the value of band gap energies values decreased, for example, from 3.05eV to 2.77 eV, which shows the visible light's capability of absorption (Asad Ali et al , 2021). The varion band gap energy with Sr and Ca doped ions is illustrated in Figures 4. 5. Figure 4.5 shows the energy band gap varies for the doping of Sr and Ca ions by interchanging in the sample. Sev eral properties, like the particle size, dopant, and preparation method, affect the material's optical band gap (Mamman et al. , 2021). The material, which include high band gap, is perfect for sola r applications. The optical band gap varies with the calcium value for all samples. Such that

varies in the concentration of calcium then the energy band gap increase. The band gap energy is shown in Table 4.4, which increases gradually with an increase in the Ca concentration percent and a decrease in the Sr concentration.

The bandwidth of the conduction and valance bands increased as the concentration of calcium increased, resulting in the band gap from the table 4.4. The band gap value increases with an increase in the concentration of calcium and a decrease in strontium concentration, which means the energy levels within the bands are increased and each electron requires less energy to jump from the valence band to the conduction band.

$$\alpha = \frac{A(hv * Eg)^2}{hv}$$

The material's optical band gap is influenced by a number of factors, including preparation technique, dopant, and particle size. The material is ideal for solar applications because of its high band gap. For every sample, the optical band gap changes with the calcium value. When the calcium concentration fluctuates, the energy band gap widens. Table 4.1 and 4.2 displays the band gap energy, which progressively rises as the percentage of Ca concentration increases and the percentage of Sr concentration decreases.

The decrease in the optical band gap of barium hexaferrite when doped with strontium and calciu m can be attributed to various factors such as changes in the electronic structure, crystal lattice parameters, and the formation of defects within the material. When strontium concentration decreases and calcium concentration increases, the following mechanisms may be involved

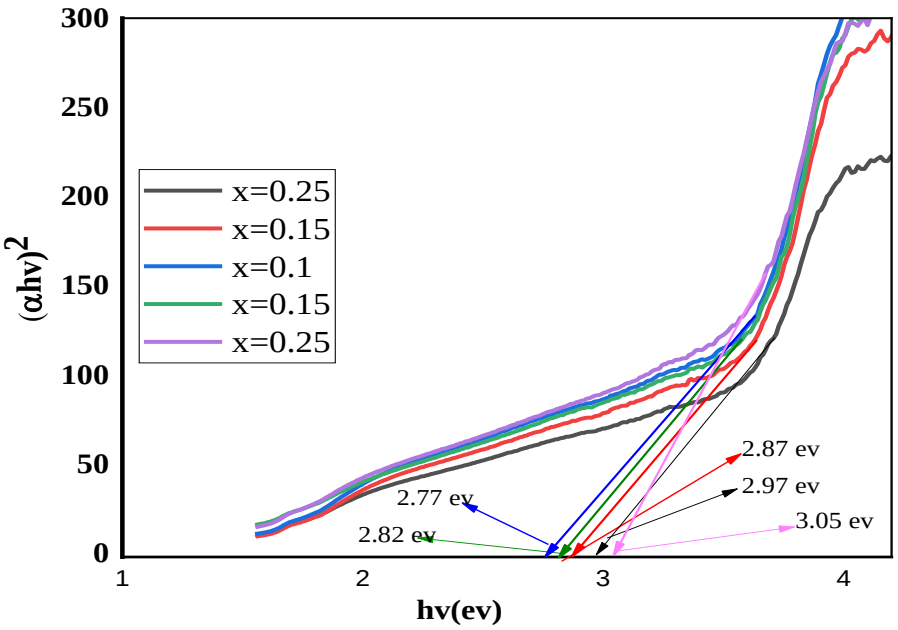

Figure 4.5: Taues plots for optical energy band gap of $Ba_{0.75}Sr_{x}$-$_{0.25}Ca_{x}Fe_{12}O_{19}$ hexaferrites

Strontium (Sr) and calcium (Ca) are likely substituting for barium hexaferrite $BaFe_{12}O_{19}$ in the crystal lattice of barium hexaferrite. Both strontium and calcium ions have different ionic radii compared to barium ions, which can lead to lattice distortions and changes in the electronic structure. The size difference between strontium and calcium may lead to different degrees of lattice distortion and hence affect the band gap differently.

Based on the experimental and theoretical results, optimize the doping concentrations of strontium and calcium to achieve the desired optical properties, such as a specific band gap value or enhanced optical absorption in a particular spectral range.

Table 4.4 optical band gap of the $Ba_{0.75}Sr_{0.25-x}Ca_xFe_{12}O_{19}$

No	Sr-Ca concretion	Energy band gap
1	Sr (0.25), Ca (0.0)	2.97 ev
2	Sr (0.2), Ca (0.05)	2.87 ev
3	Sr (0.15), Ca (0.1)	2.83 ev
4	Sr (0.1), Ca (0.15)	2.77ev
5	Sr (0.0), Ca (0.25)	2.98 ev

Based on the experimental and theoretical results, optimize the doping concentrations of strontium and calcium to achieve the desired optical properties, such as a specific band gap value or enhanced optical absorption in a particular spectral range. Utilize various characterization techniques such as X-ray diffraction (XRD), to study the crystal structure, and chemical composition of the doped samples, providing complementary information to understand the doping effects.

CHAPTER FIVE

CONCLUSION AND RECOMMENDATION

5.1 CONCLUSION

The M type barium hexaferrite are successfully by the sol gel aut combustion. All absorption bands broadened along with a shift to lower wavenumber with the increase in the $Ca^{2+}Sr^{3+}$ content in the compound. The doping of strontium and calcium in barium hexaferrite induces significant changes in its structural and optical properties. The lattice parameters 'a' and 'c' increase, leading to an expansion of the unit cell volume, while the average crystallite size decreases. This results in a shift towards lower wave numbers in the X-ray diffraction spectrum. Furthermore, Fourier-transform infrared spectroscopy indicates that the doping predominantly affects the octahedral sites in the high-frequency range. Additionally, the optical band gap varies with increasing calcium concentration, as observed through UV-visible spectroscopy. These findings highlight the tunability of barium hexaferrite's properties through doping, suggesting its potential for applications in diverse fields such as magnetic and optical devices.

5.2. RECOMMENDATION

Further exploration into the optimal doping concentrations of strontium and calcium could be beneficial to maximize the desired structural and optical properties. This optimization could involve systematic studies to understand the effects of varying doping levels on the lattice parameters, unit cell volume, and optical band gap.

Employing controlled synthesis techniques such as sol-gel, auto combustion methods could enhance the uniformity and purity of the doped barium hexaferrite samples. These techniques offer precise control over doping concentrations and particle size, which can influence the final properties.

Considering the tunable properties of doped barium hexaferrite, tailoring the doping levels based on specific application requirements could be advantageous. For instance, adjusting the doping concentrations to optimize magnetic or optical properties for targeted applications in data storage electromagnetic devices.

REFERENCE

Agrawal J. M. (2021). Synthesis, characterization and optical properties. *IOP Conf. Series: Materials Science and Engineering, 1120 (2021)* (doi:10.1088/1757 899X/1120/1/01200 3), 012003.

Ajitanshu Vedrtnam K. (2020). A comprehensive study on structure, properties, synthesis and. *AIMS Materials Science, , 7(6)*(DOI: 10.3934/matersci.2020.6.800) 800–835.

Ali1 H. T. (2021). Tailoring the optical and magnetic properties of La-BaM. *Chinese Physical Society and IOP Publishing Ltd, 31 (DOI 10.1088/1674-1056/ac1412), 027502.*

Asad Ali S. U. (2021). Structural Optical and Microwave Dielectric. *Taif(https://doi.org/10.212 03/rs.3.rs-566760/v1), 1-13.*

Awad, M. R. (2019 December). Influence of cobalt addition and calcination temperature on the. *Mater. Res. Express 7 (2020) 015057 ,10.1088(https://doi.org/10.1088/2053 1591/ab65d e), 2053-1591.*

Ayana Ghosh D. (20199). Electronic and Magnetic Properties. *9*(10.1038/s41598-018-37339-3), 194.

Basha D. B. (2022). Structural, electrical, and magnetic properties of. *(https://doi.org/10.21203/r s.3.rs-1420921/v1), 1-41.*

Berku E. (2021). Investigation of Ferrimagnetic Sr-hexaferrite Nanocrystals for Clinical. *materials science (medžiagotyra)*.27

Brightlin B.C. (2016). Magnetic, Micro structural, and Optical Properties. *J Supercond Nov Magn(DOI 10.1007/s10948-016-3703-z).*

Baykal. H. (2016). Synthesis and Structural and Magnetic Characterization. *Springer Science 30*(*DOI 10.1007/10948-016-3958-4) :1585–1592.*

Charmi D. Patel (2020). Influence of Co^{4+}-Ca^{2+} substitution on structural, microstructure, magnet ic electrical. *Ceramics International 46(doi.org/10.1016/j.ceramint.2020.05.326.), 24816-24830.*

Delacotte, G. W. (2018). Structure determination and crystal chemistry of large repeat mixed-layer hexaferrites. *iurj, 5(https://doi.org/10.1107/S2052252518011351), 681-698.*

Erfan Handoko1 S. (2020). Microwave absorption performance of barium. *Materials Express, 10(doi:10.1166/mex.2020.1811), 2158-5849.*

Emre Burak Ertuş (2016). Effect of ^{La3}+ and Ti^{4+} Ions on the Magnetic Properties of Barium Hexaferrite. *NPG Asia Materials, 21(4), 496-502.*

ERTUĞ, B. (2021). *Investigation of Ferrimagnetic Sr-hexaferrite Nanocrystals for Clinical* (Vol. 27). Turkey, Turkey: ISSN 1392–1320 MATERIALS SCIENCE (MEDŽIAGOTYR.

GHULAM ASGHAR, 1. S. (2020). Enhanced Magnetic Properties of Barium Hexaferrite. *Journal of ELECTRONIC MATERIALS, , 49 No. 7, 2020*(https://doi.org/10.1007/s11664-020-08125-7).

Gorige A. J. (2023). Crystal structure and magnetic property correlations in. *Phys Scr 98 (2023)(https://doi.org/10.1088/1402-4896/acbbf3), 045807* .

Himani Joshi and ruban kumar. (2022, april 24). Investigations and Correlations of Structural, Magnetic, and Dielectric Properties of M-Type Barium Hexaferrite ($BaFe_{12}O_{19}$) for Hard Magnet Applications. *Journal of Superconductivity and Novel Magnetism, 35, 2435–2451.*

hmad Awadallah S (2015). Structural and magnetic properties of Vanadium Doped M-. *IOP Conf. Series: Materials Science and Engineering , 92*, 012006.

https://www.scirp.org/journal/articles.aspx searchcode=Virender+Pratap++Singh&searchfield=authors&page=(2018)://doi.org/10.4236/wjcmp.2018.82004) Current Review on the Synthesis and Magnetic Properties of M-Type Hexaferrites Material. *World Journal of Condensed Matter Physics, 8*.

Ibrahim Mohammed J. M. (2023). Review on Y-type hexaferrite Synthesis characterization and properties. *Applied Surface Science Advances, Volume 16*(https://doi.org/10.1016/j.apsadv.2023.100416), 100416.

Jumr. M. (2021). Synthesis, characterization and optical properties of rare earth. *Series: Materials Science and Engineering, 1120 (2021)* (doi:10.1088/1757-899X/1120/1/012003), 012003.

Ismat Bibi, T. N. (2021). Band gap tuning of $BaFe_{12}O_{19}$ with Mg and Mn doping to enhance solar light absorption for photocatalytic application. *Scientific Research(https://doi.org/10.1002/er.6600), 123.*

João Carvalheiras a R. (2019;). Synthesis of red mud derived M-type barium hexaferrites with tuneable. *46, 575-6457.*

Kar M. K. (2021). Crystal structure and magnetic properties study on barium hexaferrite. *springe r, 127(doi.org/10.1007/s00339-020-04232-8), 127:138.*

Kar M. K. (2021). The $BaFe_{12}O_{19}$ (BHF) was prepared by the sol–gel method and annealed at different temperatures (800 °C, 900 °C, 1000 °C, and 1100 °C).Magnetic properties of BHF depend on bond angles and bond lengths between Fe and O atoms at different crystallographic sit. *Applied Physics A, 127*(doi.org/10.1007/s00339-020-04232-8), 2-12.

Mahapatro, J. (2021). Synthesis, characterization and optical properties of rare earth. . *Series: Materials Science and Engineering, 1120 (doi:10.1088/1757-899X/1120/1/012003), 012003.*

Mamman Nur Sanda M. (2021). Effect of Drying Temperature on the Magnetic and Microstructu ral. *Advances in Materials Science and Engineering, 2021*(https://doi.org/10.1155/2021/ 5884308), 9.

Maramu Nyathani G. S. (2021). Crystal Chemistry Magnetic and Dielectric Properties of. *bioint erfaceresearch.com/(1,), 929 - 939.*

Martirosyan. K.S.(2010). Barium hexaferrite nanoparticles: Synthesis and magnetic properties. *www.elsevier.com/locate/mseb*(www.elsevier.com/locate/mseb), 8–13.

Misbah, I. B. (2022, September 17). Enhanced visible light-driven photocatalytic degradation of crystal violet dye using Cr doped BaFe12O19 prepared via facile micro-emulsion route. *Journal of Saudi Chemical Society, 26*(6).

Muhammad Asif Rafiq Moaz Waqar Qaisar Khushi Muhammad (2017). Conduction mechanis m and magnetic behavior of Cu doped barium. *Springer Science, 29*(doi.org/10.1007/s10 854-017-8477-y), 5134–5142.

Murli Kumar, M. (2021). Crystal structure and magnetic properties study on barium hexaferrite. *Applied Physics (2021) , 127, 138.*

Nikolenko, P & Nizamov. (n.d.). *Structure and Magnetic Properties of* $SrFe_{12-x}InxO_{19}$. (H. W. and, Ed.) *Russia: 30 December 2022.*

Packiaraj.G M. H. (.2020). Magnetic properties of Cu and Al doped nano $BaFe_{12}O_{19}$ ceramics. *Biointerface applied chemistry, 10(3,2020), 5455-5459.*

Pon D. Popa E. R. (2005). influence of calcium on properties of strontium and barium (vol. vol. 7). *Romania, Romania: Institute of Technical Physics,.*

Polina I. Nikolenko, T. R. (2023). Structure and Magnetic Properties of $SrFe_{12-x}InxO_{19}$. *material , 16*, 347.

Pooja Dhiman (2021). Hexagonal Ferrites, Synthesis, Properties and (Vol. 10). *Pietermaritzburg Campus, South Afric: Materials Research Forum LLC.*

Pooja Dhiman (2021)). *Hexagonal Ferrites, Synthesis, Properties and* (Vol. 10). Pietermaritzbur g Campus, South Afric: Materials Research Forum LLC.

Pullar, R. C. (2012). A review of the synthesis, properties. *w w w . e l s e v i e r . c o m / l o c a t e / p m a t s c i, 57, 1191–1334.*

Rewatkar, K. G. (July-201). *Structural and Dielectric Properties of* (Vol. 8). Maharashtr: International Journal of Engineering Research & Technology (IJERT).

Safia Anjum1 Fatima Sehar1 Zeeshan Mustafa M. S. Awan. (2018). Enhancement of structural and magnetic properties of M-type. *Applied Physics, 124, 49.*

Syahwina, N. M. ((2017). Synthesis of $BaFe_{12}O_{19}$ Using Templates from Starch. *International Journal of Applied Engineering Research ISSN, Volume 12, Number 4 (2017) pp. 513-518*(0973-4562).

Safia Anjum Fatima Sehar Zeeshan Mustafa M. S. Awan. ((2018). Enhancement of structural and magnetic properties of M-type. *Applied Physics, 124*, 49.

Sonal Singhal K. K. (2011). Structural and Magnetic Properties of. *World Journal of Condensed Matter Physics, 1(10.4236/wjcmp.2011.13016), 101-104.*

Sonal Singhal K. K. (2013.). Structural and Magnetic Properties of. *World Journal of Condensed Matter Physics, 2011, 1, 101-104*(10.4236/wjcmp.2011.13016), 10-106.

Syukur Daulay B. (2019). Magnetic Characterization of Manganese doped-Barium Hexaferrite. *UI Proceedings on Science and Technology, Vol. 2 2019, Vol. 2* , 53-57.

Tchouank.T Tekou Carol Amar Srivastava J. Mohammed (2020). Investigation of energy band-gap of the composite of hexaferrites and polyaniline. *SN Applied Science 2*(https://doi.or g/10.1007/s42452-020-2516-7), 864.

VadBanihashemi M. E. (2020). A study of Ca-doped hexaferrite. *Phys. Scr, 95(/10.1088/1402-4896/abac74), 095807 (11pp.*

Vadivelan N. V. (2016). Investigation of magnetic and structural properties of copper substitute d.*elsevier, 6(Results in Physics 6 (2016) 843–850), 843–850.*

Vedrtnam, A. (2020). *comprehensive study on structure, properties, synthesis and* (Vol. 7(6)). *Spain: AIMS Materials Science.*

Velmurugan, S. K. (2012). Magnetic properties of Ni–Co doped barium strontium. *J Mater Sci: Mater Electron, 23(DOI 10.1007/s10854-012-0631-y), 1575–1579.*

VERMA S. (2023). Ca-induced changes in the crystal structure and magnetic properties. *Indian Academy of Science, 46(doi.org/10.1007/s12034-023-03031-0Sadhana(0123456789().,-volV)FT3](012345 6789(012345 6789().,-v), 2 - 11* .

Virender Pratap Singh R. (2018). A Current Review on the Synthesis and. *8*, 36-61.

Virender Pratap Singh R. (2018). A Current Review on the Synthesis and. *World Journal of Condensed Matter Physics,, 8(10.4236/wjcmp.2018.82004), 36-61*.

Virender Pratap Singh R. (2018). A Current Review on the Synthesis and. *World Journal of Condensed Matter Physics,, 8(10.4236/wjcmp.2018.82004), 36-61*.

W A Chapa Pamodani Wanniarachchi1. (2024). Deep insight into structural and optoelectronic properties of mixed. *Mater. Res. Express 1, 11*(DOI 10.1088/2053-1591/ad1f98), 025901.

Yem Slimani a. (2021). Fabrication of exchange coupled hard/soft magnetic. (02992, Ed.) *Arabian Journal of Chemistry, 14*.

Yazdi M. N. (2021). Effect of Drying Temperature on the Magnetic and Microstructural. *Advances in Materials Science and Engineering, Volume 2021*(https://doi.org/10.1155/2021/5884308), 9 .

Yinghui Zhang, J. Y. (2021). The effect of grain size before cold rolling on the magnetic properties. *Mater. Res. Express 8 (2021) 016303, 8 (2021)* (10.1088/2053-1591/abdb4f), 016303.